

Full-vectorial whispering-gallery-mode cavity analysis

Xuan Du, Serge Vincent, and Tao Lu*

Department of Electrical and Computer Engineering, University of Victoria, EOW 448, 3800 Finnerty Rd., Victoria, BC, V8P 5C2, Canada

*taolu@ece.uvic.ca

<http://www.ece.uvic.ca/~taolu>

Abstract: We present a full-vectorial three-dimensional whispering-gallery-mode microcavity analysis technique. With this technique, optical properties such as resonance wavelength, quality factor, and electromagnetic field distribution of a microcavity in the presence of individual nanoparticle adsorption can be simulated with high accuracy, even in the presence of field distortion from plasmon effects at a wavelength close to plasmon resonance. This formulation is applicable to a wide variety of whispering-gallery related problems, such as waveguide to cavity coupling and full wave propagation analysis of a general whispering-gallery-mode microcavity where axisymmetry along the azimuthal direction is not required.

© 2013 Optical Society of America

OCIS codes: (230.3990) Micro-optical devices; (040.1880) Detection; (230.5750) Resonators.

References and links

1. K. Vahala, "Optical microcavities," *Nature* **424**, 839–846 (2003).
2. D. Armani, T. Kippenberg, S. Spillane, and K. Vahala, "Ultra-high-Q toroid microcavity on a chip," *Nature* **421**, 925–928 (2003).
3. S. I. Shopova, R. Rajmangal, Y. Nishida, and S. Arnold, "Ultrasensitive nanoparticle detection using a portable whispering gallery mode biosensor driven by a periodically poled lithium-niobate frequency doubled distributed feedback laser," *Rev. Sci. Instrum.* **81**, 103110 (2010).
4. J. Dominguez-Juarez, G. Kozyreff, and J. Martorell, "Whispering gallery microresonators for second harmonic light generation from a low number of small molecules," *Nat. Commun.* **2**, 1–8 (2010).
5. H. Lee, T. Chen, J. Li, K. Y. Yang, S. Jeon, O. Painter, and K. J. Vahala, "Chemically etched ultrahigh-Q wedge-resonator on a silicon chip," *Nat. Photonics* **6**, 369–373 (2012).
6. Y. Sun, J. Liu, G. Frye-Mason, S.-j. Ja, A. K. Thompson, and X. Fan, "Optofluidic ring resonator sensors for rapid dnt vapor detection," *Analyst* **134**, 1386–1391 (2009).
7. G. Bahl, X. Fan, and T. Carmon, "Acoustic whispering-gallery modes in optomechanical shells," *New J. Phys.* **14**, 115026 (2012).
8. M. R. Lee and P. M. Fauchet, "Nanoscale microcavity sensor for single particle detection," *Opt. Lett.* **32**, 3284–3286 (2007).
9. J. R. Buck and H. J. Kimble, "Optimal sizes of dielectric microspheres for cavity QED with strong coupling," *Phys. Rev. A* **67**, 033806 (2003).
10. S. M. Spillane, T. J. Kippenberg, and K. J. Vahala, "Ultralow-threshold raman laser using a spherical dielectric microcavity," *Nature* **415**, 621–623 (2002).
11. M. L. Gorodetsky, A. A. Savchenkov, and V. S. Ilchenko, "Ultimate Q of optical microsphere resonators," *Opt. Lett.* **21**, 453–455 (1996).
12. S. Arnold, M. Khoshimia, I. Teraoka, S. Holler, and F. Vollmer, "Shift of whispering-gallery modes in microspheres by protein adsorption," *Opt. Lett.* **28**, 272–274 (2003).
13. T. Lu, H. Lee, T. Chen, S. Herchak, J.-H. Kim, S. E. Fraser, R. C. Flagan, and K. Vahala, "High sensitivity nanoparticle detection using optical microcavities," *Proc. Natl. Acad. Sci. U. S. A.* (2011).

14. B. Min, E. Ostby, V. Sorger, E. Ulin-Avila, L. Yang, X. Zhang, and K. Vahala, "High-Q surface plasmon polariton whispering gallery microcavity," *Nature* **457**, 455–458 (2009).
15. S. I. Shopova, R. Rajmangal, S. Holler, and S. Arnold, "Plasmonic enhancement of a whispering-gallery-mode biosensor for single nanoparticle detection," *Appl. Phys. Lett.* **98**, 243104 (2011).
16. M. Santiago-Cordoba, S. Boriskina, F. Vollmer, and M. Demirel, "Nanoparticle-based protein detection by optical shift of a resonant microcavity," *Appl. Phys. Lett.* **99**, 073701 (2011).
17. M. A. Santiago-Cordoba, M. Cetinkaya, S. V. Boriskina, F. Vollmer, and M. C. Demirel, "Ultrasensitive detection of a protein by optical trapping in a photonic-plasmonic microcavity," *J. Biophotonics* **5**, 629–638 (2012).
18. I. Teraoka, S. Arnold, and F. Vollmer, "Perturbation approach to resonance shifts of whispering-gallery modes in a dielectric microsphere as a probe of a surrounding medium," *J. Opt. Soc. Am. B* **20**, 1937–1946 (2003).
19. M. R. Foreman and F. Vollmer, "Theory of resonance shifts of whispering gallery modes by arbitrary plasmonic nanoparticles," *New J. Phys.* **15**, 083006 (2013).
20. M. Oxborrow, "Traceable 2-D finite-element simulation of the whispering-gallery modes of axisymmetric electromagnetic resonators," *IEEE Trans. Microwave Theory Tech.* **55**, 1209–1218 (2007).
21. J. D. Swaim, J. Knittel, and W. P. Bowen, "Detection limits in whispering gallery biosensors with plasmonic enhancement," *Appl. Phys. Lett.* **99**, 243109 (2011).
22. J. Y. Lee, X. Luo, and A. W. Poon, "Reciprocal transmissions and asymmetric modal distributions in waveguide-coupled spiral-shaped microdisk resonators," *Opt. Express* **15**, 14650–14666 (2007).
23. X. Luo and A. W. Poon, "Coupled spiral-shaped microdisk resonators with non-evanescent asymmetric inter-cavity coupling," *Opt. Express* **15**, 17313–17322 (2007).
24. A. Massaro, V. Errico, T. Stomeo, R. Cingolani, A. Salhi, A. Passaseo, and M. De Vittorio, "3-d fem modeling and fabrication of circular photonic crystal microcavity," *J. Lightwave Technol.* **26**, 2960–2968 (2008).
25. A. Kaplan, M. Tomes, T. Carmon, M. Kozlov, O. Cohen, G. Bartal, and H. G. L. Schwefel, "Finite element simulation of a perturbed axial-symmetric whispering-gallery mode and its use for intensity enhancement with a nanoparticle coupled to a microtoroid," *Opt. Express* **21**, 14169–14180 (2013).
26. J. Wiersig, "Boundary element method for resonances in dielectric microcavities," *J. Opt. A: Pure Appl. Opt.* **5**, 53 (2003).
27. C.-L. Zou, Y. Yang, Y.-F. Xiao, C.-H. Dong, Z.-F. Han, and G.-C. Guo, "Accurately calculating high quality factor of whispering-gallery modes with boundary element method," *J. Opt. Soc. Am. B* **26**, 2050–2053 (2009).
28. C.-L. Zou, H. G. L. Schwefel, F.-W. Sun, Z.-F. Han, and G.-C. Guo, "Quick root searching method for resonances of dielectric optical microcavities with the boundary element method," *Opt. Express* **19**, 15669–15678 (2011).
29. T. Lu and D. Yevick, "A vectorial boundary element method analysis of integrated optical waveguides," *J. Lightwave Technol.* **21**, 1793–1807 (2003).
30. T. Lu and D. Yevick, "Boundary element analysis of dielectric waveguides," *J. Opt. Soc. Am. A* **19**, 1197–1206 (2002).
31. P. Bienstman and R. Baets, "Optical modelling of photonic crystals and vcsels using eigenmode expansion and perfectly matched layers," *Opt. Quantum. Electron.* **33**, 327–341 (2001).
32. K. Jiang and W.-P. Huang, "Finite-difference-based mode-matching method for 3-d waveguide structures under semivectorial approximation," *J. Lightwave Technol.* **23**, 4239–4248 (2005).
33. J. Mu and W.-P. Huang, "Simulation of three-dimensional waveguide discontinuities by a full-vector mode-matching method based on finite-difference schemes," *Opt. Express* **16**, 18152–18163 (2008).
34. J. Zheng and M. Yu, "Rigorous mode-matching method of circular to off-center rectangular side-coupled waveguide junctions for filter applications," *IEEE Trans. Microwave Theory Tech.* **55**, 2365–2373 (2007).
35. I. H. Malitson, "Interspecimen comparison of the refractive index of fused silica," *J. Opt. Soc. Am.* **55**, 1205–1208 (1965).
36. G. M. Hale and M. R. Querry, "Optical constants of water in the 200-nm to 200-μm wavelength region," *Appl. Opt.* **12**, 555–563 (1973).
37. X. Ma, J. Q. Lu, R. S. Brock, K. M. Jacobs, P. Yang, and X.-H. Hu, "Determination of complex refractive index of polystyrene microspheres from 370 to 1610 nm," *Phys. Med. Biol.* **48**, 4165 (2003).
38. P. B. Johnson and R. W. Christy, "Optical constants of the noble metals," *Phys. Rev. B: Condens. Matter Mater. Phys.* **6**, 4370–4379 (1972).
39. S. A. Maier, *Plasmonics: Fundamentals and Applications* (Berlin: Springer, 2007).

1. Introduction

Whispering-gallery-mode (WGM) cavities have been adopted in a wide range of applications [1–8]. By confining light energy within a mode volume on the order of hundreds to thousands of cubic microns [9, 10], WGM resonators [1, 11] can be used to sense minute local environment changes. In particular, nanoparticles adsorbed to the cavity surface will be polarized by the WGM and cause a shift of cavity resonance wavelength [12, 13]. In addition, it

has been recently reported that a localized surface plasmon resonance (LSPR) can largely enhance the sensitivity of a microcavity [14–17] by increasing the field intensity around bound plasmonic particles.

To guide research in the aforementioned fields, numerical techniques are required. Currently, a perturbative approach [18, 19] that employs two-dimensional mode solvers such as those implemented in the finite element method [20] can be adapted to predict particle induced resonance shifts of an axisymmetric WGM. This technique involves the discretization of the two-dimensional cross section of the unperturbed WGM along the transverse direction to obtain a modal field distribution while the resulting resonance wavelength shift, e.g. from nanobead adsorption events, is computed as a perturbation to the mode. This yields highly accurate results for plain nanoparticles that do not trigger significant distortion to the cavity modal field. In the event that gold nanoparticles land on the surface of a WGM cavity, the associated plasmonic effects focus the light to the proximity of the bead, hence yielding larger inaccuracy. Such inaccuracy invalidates the perturbation approach in the case of large metallic beads or at a wavelength close to the plasmon resonance [19]. To circumvent this problem, a refinement scheme for the first order perturbation approach was proposed [15, 21] to model the WGM cavities with bound plasmonic particles. By approximating the WGM using a polarized plane wave, such a scheme employs an additional optical scattering solver to refine the field surrounding the bound particles. While such a refinement scheme provides an effective solution to nanoscale plasmonic and non-plasmonic binding problems, the plane wave approximation approaches its limit for larger particles when the field across the particle is no longer uniform. Further, perturbative approaches cannot simulate the resonance wavelength and quality factor of a WGM cavity that does not exhibit axisymmetry under the current formalism [22, 23]. Alternatively, one may choose first-principle techniques that directly solves Maxwell's equations, Helmholtz equations or Green functions with numerical techniques such as finite difference, finite element or boundary element [24–30] methods to perform a full wave analysis over the three-dimensional WGM microcavities. Unfortunately, such techniques require the discretization of the WGM along all three spatial dimensions. This necessitates extensive computational resources compared to 2-D mode solver based techniques due to orders of magnitude increase in grid points. To accommodate such difficulties, first principle techniques are commonly used in conjunction with the effective index technique to approximate the three-dimensional WGM as a two-dimensional one. In [25], a new approach is proposed to simulate a WGM with a localized perturbation by treating the perturbed section of the WGM as a three-dimensional closed cavity, where artificial boundary conditions such as a perfect electrical wall are imposed at the input and output ends of the section. A three-dimensional mode of this perturbed section is then computed with the finite element method to approximate the distorted WGM field and other corresponding parameters. Such a method can yield better accuracy compared to a perturbation approach by applying a correction to the WGM field distorted by the bead. In this case, the number of grid points per computation step that are involved is larger than the perturbation approach yet fewer than first principle techniques. On the other hand the boundary condition imposed in [25], as pointed out by the authors of that article, is based on the assumption that the light scattered by the adsorbed bead will quickly "heal" within the perturbed section and that the model "represents a resonator with many particles [located periodically] along the circumference." Such an assumption no longer holds for the binding of larger beads or for beads that are located at random positions, thereupon introducing significant phase shift and amplitude distortion of the otherwise unperturbed WGM field. The field obtained from this method is a standing wave pattern of the cavity, which departs from the realistic situation where a travelling wave is involved. Furthermore, the multi-scale nature of a WGM-nanoparticle system introduces additional challenges with these methods. For a large size perturbation such as a

fiber taper placed close to the cavity, a large section is needed for the model. This causes the resulting mesh to become too large for a conventional computer to handle. Here, we modify the mode-matching method (MMM) to model WGM cavities and demonstrate its capability to address all the challenges mentioned above.

MMM has been widely used in modeling and designing straight waveguide discontinuities, junctions, and filters in Cartesian coordinates [31–34]. In MMM, the optical structure is divided into a number of slices along the propagation axis. In each slice a complete orthonormal set of eigen modes derived from an infinitely long waveguide, whose cross section along the propagation direction has an identical refractive index profile to the slice, are employed to form the basis of the solution space where an arbitrary electromagnetic (EM) field distribution can be expanded upon. The field will then be projected to the next slice along the propagation direction as if each modal field propagates with its distinct propagation constant. The new field will then be re-expanded on the eigen modes native to the new slice. The wave propagation behaviour can be simulated by progressively projecting fields via the above-mentioned approach from one slice to the next along the propagation direction. By analogy, we partition a WGM system along the azimuthal direction and obtain full vector WGM modes at each slice. Mode matching between neighbouring slices is then performed to emulate wave propagation in the WGM cavity, while optical properties such as resonance wavelength and quality factor are calculated accordingly.

2. Theoretical formulations

2.1. Ideal whispering-gallery-mode microcavities

An ideal or axisymmetric whispering-gallery-mode microcavity has a complex refractive profile $\tilde{n}(\rho, z, \phi)$ independent of the azimuthal angle ϕ (ie. $\tilde{n}(\rho, z, \phi) = \tilde{n}(\rho, z)$) in a concentric cylindrical coordinate system, as shown in Fig. 1(a). The electric field $\tilde{\mathbf{E}}(\rho, z, \phi)$ of light at wavelength λ_0 that propagates inside the cavity has the form

$$\tilde{\mathbf{E}}(\rho, z, \phi) = \tilde{A}(\phi) \cdot \hat{\mathbf{e}}(\rho, z) \quad (1)$$

where $\hat{\mathbf{e}}(\rho, z)$ is the whispering-gallery-mode profile obtainable from the corresponding mode equations

$$\left[\frac{\partial^2}{\partial \rho^2} + \frac{1}{\rho} \frac{\partial}{\partial \rho} + \frac{\partial^2}{\partial z^2} + \left(k_0^2 \tilde{n}^2(\rho, z) - \frac{\tilde{m}^2}{\rho^2} \right) \right] \hat{\mathbf{e}}(\rho, z) = \mathbf{0} \quad (2)$$

The mode profile is normalized according to the area integral at the cavity cross section normal to the $\hat{\phi}$ direction. That is, $\frac{1}{2\eta_0} \int \tilde{n}_r(\rho, z) \hat{e}^*(\rho, z) \hat{e}(\rho, z) d\sigma = 1$ such that the field amplitude square $\tilde{A}(\phi)^* \cdot \tilde{A}(\phi)$ represents the power at ϕ in units of Watts. Here $\eta_0 = 377$ Ohms is the free space impedance and $\tilde{n}_r(\rho, z)$ is the real part of the refractive index at ϕ . $\tilde{m} = \tilde{m}_r + j\tilde{m}_i$ is a constant complex number whose real part \tilde{m}_r encompasses the phase change of the wave-front and the imaginary part \tilde{m}_i characterizes the loss of the wave along the propagation direction. In the case of an ideal WGM cavity, $\tilde{A}(\phi) = \tilde{A}(\phi = 0) e^{j\tilde{m}\phi}$. When λ_0 coincides with the cavity resonance wavelength $\tilde{\lambda}_{res}$, \tilde{m}_r becomes an integer M whose value determines the azimuthal order of the mode. The loss of the cavity can be estimated by the quality factor $Q_{tot} = M/2\tilde{m}_i$ with the value contributed by cavity material absorption ($\tilde{Q}_{abs} = M/2\tilde{m}_{abs}$), radiation loss ($\tilde{Q}_{rad} = M/2\tilde{m}_{rad}$), surface roughness ($\tilde{Q}_{surf} = M/2\tilde{m}_{surf}$), and cavity to tapered waveguide coupling ($\tilde{Q}_{couple} = M/2\tilde{m}_{couple}$). Evidently,

$$\begin{aligned} \frac{1}{Q_{tot}} &= \frac{2\tilde{m}_i}{M} = \frac{1}{\tilde{Q}_{abs}} + \frac{1}{\tilde{Q}_{rad}} + \frac{1}{\tilde{Q}_{surf}} + \frac{1}{\tilde{Q}_{couple}} \\ \tilde{m}_i &= \tilde{m}_{abs} + \tilde{m}_{rad} + \tilde{m}_{surf} + \tilde{m}_{couple} \end{aligned} \quad (3)$$

2.2. Non-ideal whispering-gallery-mode microcavities

In general, a whispering-gallery-mode microcavity may have a ϕ -dependent refractive index profile $n(\rho, z, \phi)$ if particle binding occurs, surface imperfections exist, a waveguide taper is placed close to the cavity, or other geometrical disturbances are introduced. For simplicity, we drop \sim symbols for all the physical quantities to distinguish them from those defined in an ideal WGM.

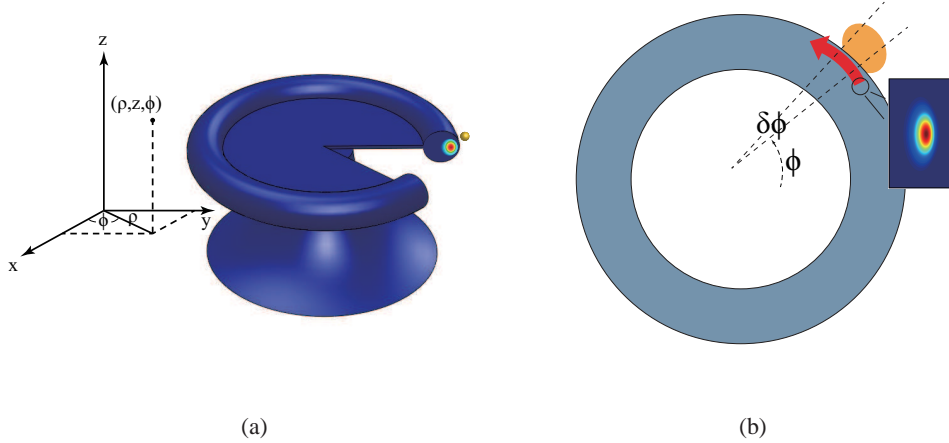


Fig. 1: (a) Light circulating along the azimuthal direction in a whispering-gallery-mode microcavity (e.g. a silica microtoroid). A cylindrical coordinate system is used for modelling purposes. (b) Light propagating from ϕ to $\phi + \delta\phi$ as it passes by a bound particle.

At an azimuthal angle ϕ_0 , the electrical field distribution at the cross section $\mathbf{E}(\rho, z, \phi_0)$ can be expanded onto the normalized WGM mode $\hat{\mathbf{e}}(\rho, z, \phi_0)$ at ϕ_0 according to

$$\mathbf{E}(\rho, z, \phi_0) = A(\phi_0) \cdot \hat{\mathbf{e}}(\rho, z, \phi_0) \quad (4)$$

Note that by analogy to the MMM in Cartesian coordinates, we may obtain a complete set of orthogonal modes at the azimuthal angle ϕ_0 that satisfies the mode equation of a perfect WGM cavity

$$\left[\frac{\partial^2}{\partial \rho^2} + \frac{1}{\rho} \frac{\partial}{\partial \rho} + \frac{\partial^2}{\partial z^2} + \left(k_0^2 n^2(\rho, z, \phi_0) - \frac{m(\phi_0)^2}{\rho^2} \right) \right] \hat{\mathbf{e}}(\rho, z, \phi_0) = \mathbf{0} \quad (5)$$

where both the mode profile and m have become ϕ -dependent. Additionally, given that (5) is identical to (2) for any fixed angle ϕ_0 , one may find the M^{th} order resonant wavelength $\lambda_r(\phi)$ at ϕ_0 by replacing k_0 with $2\pi/\lambda_r$, m with M , and solving the mode equation above using a two-dimensional mode solver for ideal WGM's (such as that in [20]). Note $\lambda_r(\phi)$ is also a ϕ -dependent quantity. After propagating an infinitesimal azimuthal angle $\delta\phi$ (Fig. 1(b)), we obtain the electrical field at $\phi_0 + \delta\phi$

$$\mathbf{E}(\rho, z, \phi_0 + \delta\phi) = A(\phi_0) \cdot \hat{\mathbf{e}}(\rho, z, \phi_0) e^{jm(\phi_0)\delta\phi} \quad (6)$$

Under the approximation that, on average, photons in the mode travel the same optical path length and experience the same loss as those at the resonance wavelength $\lambda_r(\phi_0)$, we can obtain

the real m_r and imaginary m_i part of $m(\phi_0)$ after infinitesimal rotation $\delta\phi$ via

$$\begin{aligned} m_r(\phi_0) &= M \frac{\lambda_r(\phi_0)}{\lambda_0} \\ m_i(\phi_0) &= m_{abs}(\phi_0) + m_{rad}(\phi_0) \end{aligned} \quad (7)$$

Here, we ignore m_{couple} and m_{surf} for a purpose explained in a later section. On the other hand, $\mathbf{E}(\phi_0 + \delta\phi)$ can be expanded onto the normalized eigen mode $\hat{\mathbf{e}}(\rho, z, \phi_0 + \delta\phi)$, defined at $\phi_0 + \delta\phi$,

$$\mathbf{E}(\rho, z, \phi_0 + \delta\phi) = A(\phi_0 + \delta\phi) \cdot \hat{\mathbf{e}}(\rho, z, \phi_0 + \delta\phi) \quad (8)$$

By equating the right hand sides of (6) and (8), multiplying both sides by $\frac{1}{2\eta_0} n_r(\rho, z, \phi_0 + \delta\phi) \hat{\mathbf{e}}(\rho, z, \phi_0 + \delta\phi)$, and integrating over the cross section at $\phi_0 + \delta\phi$, we obtain the evolution of $A(\phi_0 + \delta\phi)$ according to

$$A(\phi_0 + \delta\phi) = A(\phi_0) \cdot e^{j[M + \delta m(\phi)]\delta\phi} \quad (9)$$

We may then obtain an additional loss term $m_m(\phi_0)$ characterized by

$$m_m(\phi_0) = - \lim_{\delta\phi \rightarrow 0} \frac{1}{\delta\phi} \ln \left[\int \frac{n_r(\rho, z, \phi_0 + \delta\phi)}{2\eta_0} \hat{e}^*(\rho, z, \phi_0 + \delta\phi) \hat{e}(\rho, z, \phi) d\sigma \right] \quad (10)$$

arising from the mode mismatch between $\hat{e}(\phi_0 + \delta\phi)$ and $\hat{e}(\phi_0)$ in addition to the absorption and radiation loss derived from m_i . For simplicity, we redefine $m_i(\phi_0) = m_m(\phi_0) + m_{abs}(\phi_0) + m_{rad}(\phi_0)$ and define a mode order detuning term $\delta m(\phi) = [m_r(\phi) - M] + jm_i(\phi)$. Consequently, the field $\mathbf{E}(\rho, z, 0) = A(0) \hat{\mathbf{e}}(\rho, z, 0)$ propagating from $\phi = 0$ to an azimuthal angle ϕ_0 can be expressed as

$$\mathbf{E}(\rho, z, \phi_0) = A(0) e^{j[M\phi_0 + \int_{\phi=0}^{\phi_0} \delta m(\phi) d\phi]} \hat{\mathbf{e}}(\rho, z, \phi_0) \quad (11)$$

To satisfy the resonance condition, the overall phase change of the field after propagating through a 2π azimuthal angle should be $2M\pi$:

$$\int_{\phi=0}^{2\pi} m_r(\phi) d\phi = 2M\pi \quad (12)$$

Together with (7) we obtain the resonance wavelength of the whispering-gallery-mode microcavity λ_{res} by simply taking the arithmetic mean of the resonance wavelengths $\lambda_r(\phi)$ at each cross section of the cavity, where $\lambda_r(\phi_0)$ at each ϕ_0 can be obtained from the WGM mode solver for the case of an ideal WGM whose cross-sectional refractive index profile is identical to that at ϕ_0 .

$$\lambda_{res} = \frac{\int_0^{2\pi} \lambda_r(\phi) d\phi}{2\pi} \quad (13)$$

It is worth emphasizing that the simple expression in (13) is valid for all whispering-gallery-mode microcavities, including those with or without axisymmetric properties, those that are subject to dielectric or metallic particle binding, or those in the presence of a tapered fiber or any other structures. The equation above can be further simplified if the perturbation or non-axisymmetric parts of the microcavity are localized to a small region, as is demonstrated in the application section below. Similarly, one may derive the overall quality factor of an asymmetric or perturbed WGM cavity from the algebraic average of the imaginary part of δm as

$$\begin{aligned} \frac{1}{Q_{tot}} &= \frac{2 \int_0^{2\pi} [m_m(\phi) + m_{abs}(\phi) + m_{rad}(\phi)] d\phi}{2\pi M} \\ &= \frac{1}{Q_m} + \frac{1}{Q_{abs}} + \frac{1}{Q_{rad}} \end{aligned} \quad (14)$$

As can be seen, in the absence of the axisymmetry, an additional loss term from the mode mismatch between neighbouring cross sections occurs. This yields the decrease of overall Q_{tot} factor from the inclusion of the mode mismatch Q_m .

3. Application and discussion

3.1. The ideal WGM cavity

To validate the formulated algorithm, we first examine the case of a WGM with perfect axisymmetry. It's evident that the WGM mode at each cross section is identical and that the mode mismatch loss vanishes. In addition, λ_r is identical at any azimuthal angle ϕ and the cavity resonance wavelength $\lambda_{res} = \lambda_r$. Therefore, an ideal WGM cavity can be treated as a special case under the current MMM formulation.

In the presence of a tapered waveguide that couples the light in and out of the cavity, mode mismatch occurs within the cavity-taper interaction regime. The coupling loss can be viewed as a special case of mode mismatch loss triggered by the waveguide taper. Assuming the taper interacts with the cavity within an azimuthal angle between ϕ_0 and $\phi_0 + \Delta\phi$, we obtain a new formulation of coupling Q as

$$\frac{1}{Q_{coupling}} = \frac{2 \int_{\phi_0}^{\phi_0 + \Delta\phi} m_m(\phi) d\phi}{2\pi M} \quad (15)$$

By treating the tapered waveguide as part of an asymmetric WGM cavity, one may easily obtain a resonance wavelength shift $\Delta\lambda = \lambda_{res} - \tilde{\lambda}_{res}$ due to the perturbation of the waveguide taper to the cavity according to

$$\Delta\lambda = \frac{\int_{\phi_0}^{\phi_0 + \Delta\phi} [\lambda_r(\phi) - \tilde{\lambda}_{res}] d\phi}{2\pi} \quad (16)$$

Surface roughness of the cavity often contributes to the loss as an individual term [11] in the context of MMM, wherein the loss also originates from the mode mismatch between cavity cross sections. Using the same approach, one can obtain the surface roughness associated Q using the equations obtained above, although an integral over a 2π azimuthal angle must be performed. Evidently, the surface roughness could perturb optical path length and yield an addition shift of cavity resonance wavelength. This shift, however, would usually be small in magnitude.

3.2. Nanoparticles on a WGM cavity

In this test case we examine the resonant wavelength shift and decrease of quality factor when N nanoparticles land on the surface of a WGM cavity. Here we assume each nanoparticle i occupies a space lying between ϕ_i and $\phi_i + \Delta\phi_i$. From (13) and (14) we derive that the particle induced resonance wavelength shift $\Delta\lambda$ and quality factor Q change follows the expression

$$\Delta\lambda = \frac{\sum_{i=1}^N \int_{\phi_i}^{\phi_i + \Delta\phi_i} [\lambda_r(\phi) - \tilde{\lambda}_{res}] d\phi}{2\pi} \quad (17)$$

$$\frac{1}{Q_{tot}} - \frac{1}{\tilde{Q}_{tot}} = \frac{2 \sum_{i=1}^N \int_{\phi_i}^{\phi_i + \Delta\phi_i} [m_m(\phi) + m_{abs}(\phi) + m_{rad}(\phi) - \tilde{m}_i] d\phi}{2\pi M} \quad (18)$$

Equations (17) and (18) are numerically verified at an operational wavelength around 633 nm on a silica microtoroid platform [2]. The silica microtoroid under investigation has a major radius of 40 μm and a minor radius of 5 μm . The surrounding environment is filled with water. Polystyrene (PS) beads and gold (Au) beads are individually placed on the toroid equator

and the refractive indices of silica ($1.457+(6.95 \times 10^{-11})j$), water ($1.33168+(1.47 \times 10^{-8})j$), PS ($1.583+(5.29 \times 10^{-4})j$), and Au ($0.1834+3.433j$) are taken from literature [35–38]. We employed a full vector finite element whispering-gallery-mode solver according to [20] to obtain the mode at each cross section. The computation domain was meshed adaptively in order to improve the accuracy of the calculated eigen value. The trapezoidal rule is implemented to perform the integral (17) and (18) numerically to get the total resonant wavelength shift and Q factor degradation of the hybrid cavity mode. Note that for the same mesh density, [25] requires approximately 90 times more grid points than MMM in each computation step assuming a minimum-size slice of a half-wavelength in length along the cavity edge was adopted in [25]. It is demonstrated that one typical MMM simulation of a hybrid WGM-NP system for a 20-nm radius gold bead takes 33 seconds for a relative error of the calculated resonance shift around 0.3 when only two slices along the azimuthal angle are involved. Higher accuracy can be achieved with more densely packed slices along the azimuthal direction and a more accurate mode solver. Note that the calculation is not based on the same mesh scheme as in [25] as our algorithm only requires a two-dimensional mesh at each computation step.

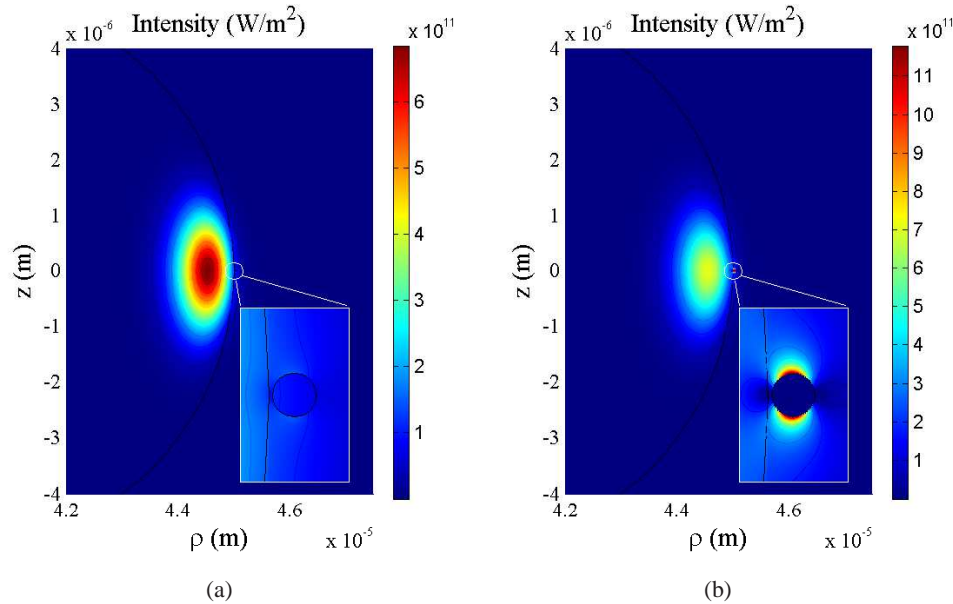


Fig. 2: The fundamental mode intensity distribution of a silica microtoroid with (a) a polystyrene bead and (b) a gold bead bound to the equator at a 633-nm wavelength. The modes are plotted at the azimuthal cross section where the center of the bead is located. The insets provide a zoomed-in view of the intensity distribution around the beads.

Figure 2 shows the intensity of the normalized toroid-bead hybrid modes at the azimuthal cross section, where the center of the beads are located. As shown in Fig. 2(a), where a polystyrene bead was adsorbed at the equator of the toroid, the intensity around the bead (c.f. Fig. 2(a) inset) displays little distortion from the unperturbed toroid mode. In this case, the resulting resonance shift of the cavity can be extracted with sufficient accuracy using first order perturbation theory [18]. Fig. 2(b) shows the WGM-SP hybrid mode excited at the gold-dielectric interface. As shown in Fig. 2(b)'s inset, there is strong field intensity stored in the surface plasmon resulting in two hot spots aligned along the same direction as that of the electric field (along the \hat{z} direction displayed for the TE mode). Due to the coupling of the WGM

and the SP, the field intensity outside the cavity is stronger than that inside the cavity. Such significant distortion to the WGM precludes the treatment of such problems with first order perturbation theory. On the other hand, MMM intrinsically incorporates the change in mode field distribution and yields accurate evaluations of the perturbed system.

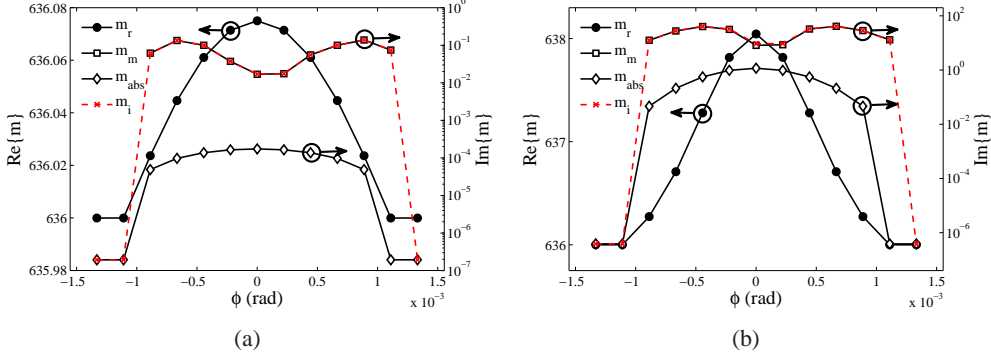


Fig. 3: The real and imaginary part of the mode order m along the propagation direction when (a) a 50-nm radius PS bead and (b) a 50-nm radius Au bead are placed at $\phi = 0$.

Figure 3 illustrates the calculated terms m_r , m_m , and m_{abs} arising from the PS (Fig. 3(a)) and gold (Fig. 3(b)) nanoparticles. It is observed that the mode mismatch loss dominates the degradation of the Q factor over material absorption in both cases.

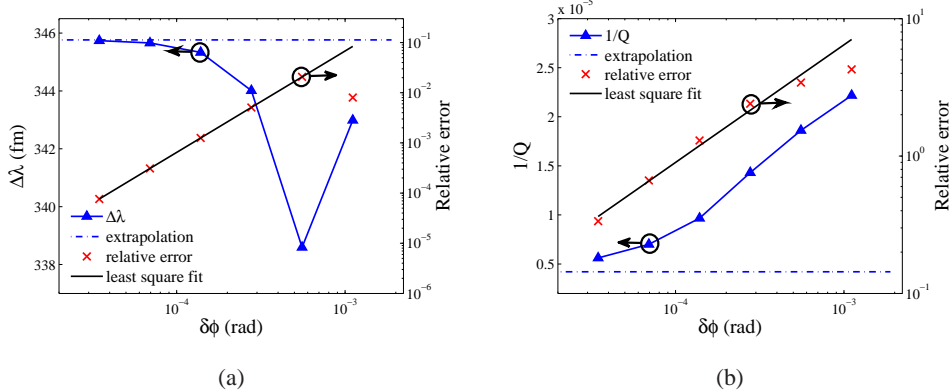


Fig. 4: Shift and Q factor vs. grid spacing $\delta\phi$ along the $\hat{\phi}$ direction for a 50-nm radius gold bead. The last point is omitted for the creation of the line of best fit.

In Fig. 4 we further investigate the convergence rate as a function of azimuthal angle discretization in the case of a 50-nm radius gold bead binding to the toroid. The percent error was calculated by comparing the results of each $\delta\phi$ to the expected result obtained through the Richardson extrapolation procedure. One can observe that the simulated resonance wavelength shift converges on the order of $O(\delta\phi^2)$ (black line in Fig. 4(a)) while the convergence rate of Q is $O(\delta\phi^{0.9})$ (black line in Fig. 4(b)). A higher convergence rate is possible by implementing higher order integration procedures to evaluate (17) and (18).

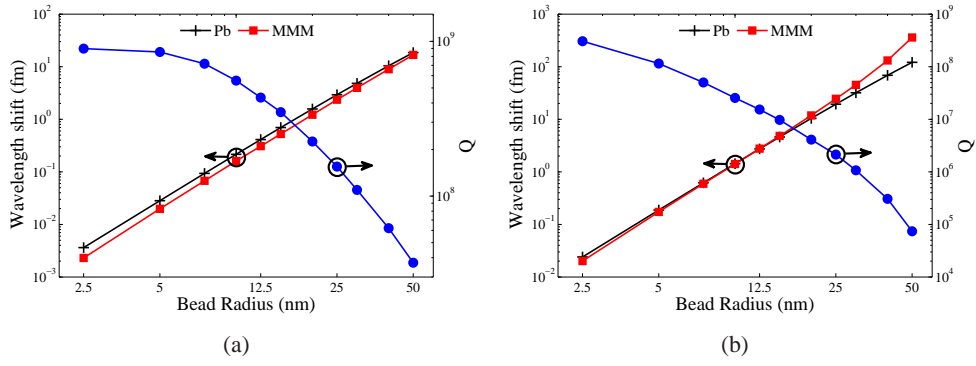


Fig. 5: Binding shift and Q factor degradation due to (a) a bound PS sphere and (b) a bound Au sphere for different bead radii.

In Fig. 5, we display the resonance wavelength shifts and the degraded Q factors due to the binding of a polystyrene (Fig. 5(a)) and gold (Fig. 5(b)) bead of different radii, where an unperturbed toroid has a resonant wavelength of 632.747 nm and a theoretical Q factor of 1.65×10^9 . The resonance shifts predicted by MMM (red solid square markers) are compared with those predicted by a first order perturbation method (black plus symbol markers). For PS beads, MMM predicts wavelength shifts which are in good agreement with those predicted by the first order perturbation method. The quality factor (blue solid circle markers) of the toroid is unaffected when a bead with radius smaller than 5 nm is attached to the surface, yet there is a drop to approximately 10^7 if a 50-nm radius bead is attached instead. The calculated wavelength shift and quality factor degradation is in line with the experimental observation reported in [13].

For the case of a gold bead simulation, the excess polarizability is given by $\alpha = 4\pi R^3 \epsilon_m (\epsilon_p - \epsilon_m) / (\epsilon_p + 2\epsilon_m)$ [39] where ϵ_p and ϵ_m are the permittivities of the particle and the medium, respectively. MMM predicts resonance shifts from 2×10^{-2} to 359 fm and Q factor degradation from 3×10^8 to 7.5×10^4 when the attached gold bead radius increases from 2.5 nm to 50 nm. As expected, at an off-plasmon resonance wavelength of 633 nm, the perturbation method matches the MMM results when the bead size is below 20 nm yet for large beads yields greater errors due to the non-negligible field distortion from the bead.

In Fig. 6 we also compared the shifts calculated by the two methods as a function of wavelengths. As illustrated, near the surface plasmon resonance of a gold nanobead (540 nm, as shown in the insert), the accuracy of the perturbation method drops below 50% due to the strong surface plasmon effect that was similarly observed in [19].

To verify our formulation we further compared our results with reported experiments. We simulated the binding of 27.5-nm gold beads to a 50- μ m radius microsphere with a 4 nm interparticle gap as reported in [16, 17]. In this simulation, we obtained a resonance wavelength shift of 32.6 fm per bead adsorption. Compared to the total resonance shift in Fig. 1(d) of [16], we predict that a total of 10 beads are adsorbed to the microsphere surface. Knowing that an unperturbed cavity quality factor of 3×10^6 was reported in the same paper, we estimated that the quality factor will drop to 5.8×10^5 by the adsorption of 10 beads. This value is in good agreement with the reported experimental value on the order of 10^5 .

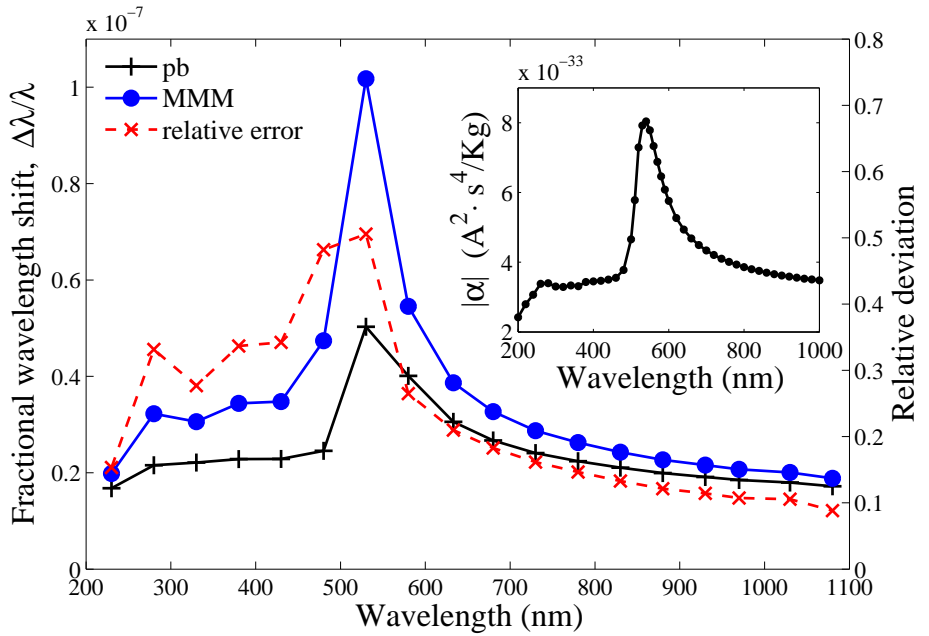


Fig. 6: Cavity resonance shifts as a function of wavelengths for a 25-nm radius gold bead. The insert shows the excess polarizability of the bead at different wavelengths.

It is worth noting that the MMM developed in this paper assumes that the cavity operates in a single whispering-gallery-mode. In practice, a WGM may contain multiple propagating modes and so omitting the coupling between different modes could decrease the accuracy of the model. A MMM formulation involving multiple WGM modes is possible, albeit at the expense of higher computational resource requirements.

4. Conclusion

A FEM based mode-matching method (FEM-MMM) has been developed for solving three-dimensional whispering-gallery-mode cavity problems. To demonstrate the validity of the method, numerical results for a microtoroid bound with a plasmonic and non-plasmonic bead were presented. Results obtained in this paper are consistent with those obtained through perturbation theory or experimental demonstration. The investigation of MMM with the inclusion of higher order modes will be carried out in forthcoming publications.